

Solving Constrained Optimization Problems Using Hybrid Qubit-Qumode Quantum Devices

Rishab Dutta,¹ Brandon Allen,¹ Nam P. Vu,^{1,2,3} Chuzhi Xu,¹ Kun Liu,⁴ Fei Miao,⁵ Bing Wang,⁵ Amit Surana,⁶ Chen Wang,⁷ Yongshan Ding,^{4,8,9} and Victor S. Batista^{1,9}

¹*Department of Chemistry, Yale University, New Haven, CT, USA 06520*

²*Department of Chemistry, Lafayette College, Easton, PA, USA 18042*

³*Department of Electrical and Computer Engineering, Lafayette College, Easton, PA, USA 18042*

⁴*Department of Computer Science, Yale University, New Haven, CT, USA 06520*

⁵*School of Computing, University of Connecticut, Storrs, CT, USA 06269*

⁶*RTX Technology Research Center, East Hartford, CT, USA 06118*

⁷*Department of Physics, University of Massachusetts-Amherst, Amherst, MA, USA 01003*

⁸*Department of Applied Physics, Yale University, New Haven, CT, USA 06520*

⁹*Yale Quantum Institute, Yale University, New Haven, CT, USA 06511*

Variational Quantum Algorithms (VQAs) offer a promising approach for solving complex optimization problems on near-term quantum hardware. In this work, we show how hybrid qubit-qumode quantum devices can address Quadratic Unconstrained Binary Optimization (QUBO) problems using the Echoed Conditional Displacement Variational Quantum Eigensolver (ECD-VQE). Leveraging circuit quantum electrodynamics (cQED) architectures, we encode QUBO instances into multiple qumodes weakly coupled to a single qubit and extract solutions directly from photon-number measurements. As a demonstration, we apply ECD-VQE to the Binary Knapsack Problem and find that it outperforms the Quantum Approximate Optimization Algorithm (QAOA) implemented on conventional qubit circuits. These results highlight the potential of ECD-VQE for a broad class of NP-hard problems. We conclude that hybrid qubit-qumode platforms can efficiently realize variational ECD ansatze that would otherwise require deep circuits on standard qubit-based quantum computers, positioning them as promising candidates for constrained optimization in early fault-tolerant quantum computing.

I. INTRODUCTION

Variational Quantum Algorithms (VQAs) represent a powerful class of hybrid quantum-classical methods designed to solve optimization problems on near-term and early fault-tolerant quantum devices.^{1–4} VQAs address such problems by encoding them into a Hamiltonian and iteratively minimizing its expectation value through classical optimization over a parametrized quantum ansatz. Their broad applicability has been demonstrated across a wide range of domains, including molecular property prediction,^{5,6} RNA folding,⁷ protein-ligand docking,⁸ machine learning,⁹ structural design,¹⁰ vehicle routing,¹¹ and capital budgeting.¹² Critically, the performance of a VQA is influenced by the expressiveness and structure of the chosen ansatz. Therefore, the exploration of powerful ansatze is a subject of great current interest.

Two well-known VQAs, the Variational Quantum Eigensolver (VQE),^{2,3,13} and the Quantum Approximate Optimization Algorithm (QAOA)^{14,15} illustrate the diversity in ansatz design strategies. VQE, originally developed for quantum chemistry applications, employs either a general ansatz agnostic to the problem Hamiltonian or chemically inspired constructions such as the unitary coupled cluster (UCC) ansatz.^{16,17} In contrast, QAOA, designed for constrained optimization, constructs its ansatz directly from the problem Hamiltonian, augmented by a non-commuting mixing Hamiltonian. While both algorithms share the objective of minimizing Hamiltonian expectation values, their ansatz structures reflect their

distinct application domains. Crucially, algorithm performance is highly sensitive to ansatz choice, which can lead to optimization challenges such as barren plateaus and local minima in the variational landscape.^{18–21} These limitations have spurred the development of alternative strategies, including quantum imaginary-time evolution methods,^{22,23} and the exploration of new ansatz architectures and quantum platforms – such as the circuits for hybrid qumode-qubit circuits investigated in this work.^{24,25}

Qumodes—quantum harmonic oscillators with an infinite-dimensional Hilbert space—offer powerful resources beyond conventional two-level qubits.²⁶ Their expressive capacity has driven the development of optimization algorithms^{27–30} tailored to qumode-only photonic systems,^{31–33} built on platforms such as integrated photonics and Gaussian boson sampling.^{31–33}

While photonic quantum computing faces challenges in realizing qumode gates beyond Gaussian unitaries, circuit quantum electrodynamics (cQED) devices enable efficient implementations.^{34,35} Specifically, in cQED, the coupling between qumodes and qubits enables efficient implementation of non-Gaussian operations, which are essential for universal quantum computation. Thus, we focus on the hybrid qubit-qumode cQED platforms here, which offer a promising path toward early fault-tolerant quantum computing. Notably, these platforms have already achieved quantum error correction beyond the break-even point for both logical qubits³⁶ and qudits.³⁷

Hybrid cQED devices, built from microwave cavity resonators coupled to transmon qubits,^{34,35} enable

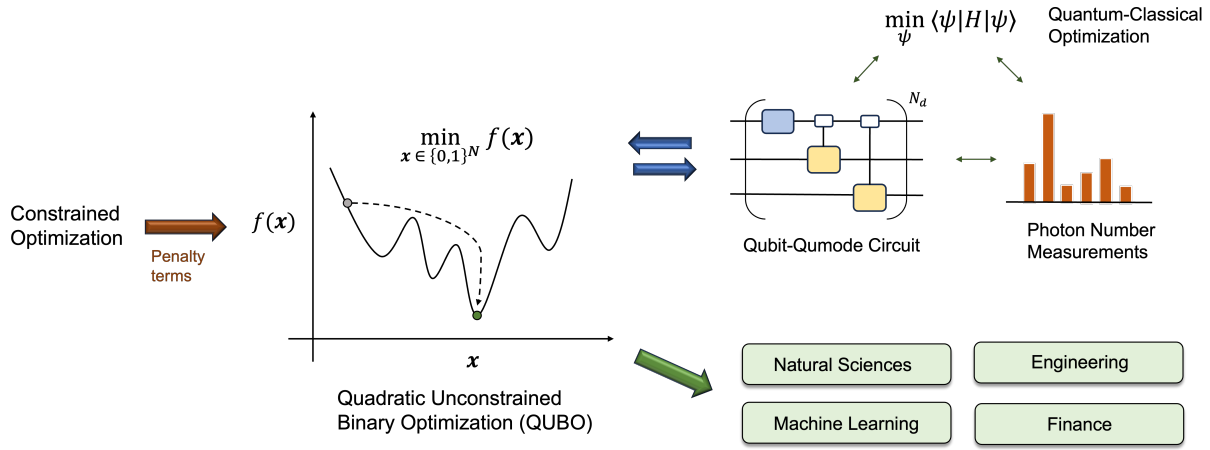


FIG. 1. A constrained optimization problem is reformulated as a QUBO instance and solved using a qubit-qumode device. The problem is encoded into a qubit-qumode Hamiltonian whose ground state corresponds to the optimal solution. This ground state is approximated via variational optimization of the circuit parameters, and the solution is read out through photon-number measurements.

high-fidelity universal gate sets^{38–42} and exhibit intrinsic noise resilience.^{36,37} Crucially, they support expressive ansatzes composed of native operations—such as sequences of echoed conditional displacement (ECD) gates combined with qubit rotations,^{39,41,42} SNAP gates interleaved with displacements and beamsplitters,^{38,43} and conditional-not displacement gates.⁴⁰ These hybrid operations enable efficient exploration of large Hilbert spaces,⁴² often with significantly fewer resources than required by qubit-only circuits,^{43,44} making them a compelling architecture for near-term quantum applications.

In this work, we apply hybrid qubit-qumode circuits to solve Quadratic Unconstrained Binary Optimization (QUBO) problems—an NP-hard class with relevance across logistics, scheduling, finance, materials discovery, and drug development.^{45–47} In machine learning, QUBO formulations address models such as support vector machines, clustering algorithms, and probabilistic graphical models.⁴⁸ Here, we introduce QUBO formulations with both soft and hard constraints using ECD-VQE, a variational quantum algorithm that leverages a hybrid ansatz composed of echoed conditional displacement (ECD) gates and qubit rotations.^{49,50} ECD-VQE encodes the QUBO Hamiltonian across multiple qumodes, each weakly coupled to a single qubit, enabling a compact and expressive representation of the problem landscape. The circuit parameters are optimized classically, while the binary decision variables are extracted from photon-number measurements on the qumodes.

We benchmark ECD-VQE on instances of constrained optimization problems and demonstrate that it outperforms the Quantum Approximate Optimization Algorithm (QAOA) on the Binary Knapsack Problem (BKP),⁵¹ both in solution quality and in navigating the optimization landscape. For the BKP, ECD-VQE reliably identifies the optimal solution with 100% probability in about 80 iterations. In contrast, QAOA fails to

exceed a 12% probability of reaching the optimal state, even with the same number of variational parameters, more iterations, and 50 independent parameter initializations. Notably, ECD-VQE achieves this performance using just 10 ECD gates native to the qubit-qumode device with only two qumodes coupled to one qubit. Reproducing equivalent unitaries on a qubit-only architecture would require 930 CNOT gates on a seven-qubit circuit, even in the best-case scenario, as discussed in Section III, highlighting the resource efficiency and expressiveness of the hybrid approach.

The remainder of the paper is organized as follows. In Section II, we describe the mapping of constrained optimization problems onto a hybrid qubit-qumode Hamiltonian and detail the ECD-VQE circuit architecture. Section III applies the method to benchmark instances of optimization problems. In Section IV, we evaluate the performance of the algorithm under simulated noise. Finally, Section V concludes with a summary of our findings and discusses directions for future work.

II. METHODS

In this section, we review how to represent a constrained optimization problem in terms of a qubit Hamiltonian before discussing how to implement it on a qubit-qumode device. Then, we introduce a variational approach to find the optimal solution as the ground state of the qubit Hamiltonian.

A. Qubit Hamiltonian

Let us review how to transform a constrained optimization problem into a QUBO form for the binary knap-

sack problem (BKP), a fundamental integer programming problem in combinatorial optimization and operations research.⁵¹ It can be defined as

$$\max_{\mathbf{x}} V = \sum_{j=0}^{N_0-1} v_j x_j, \quad x_j \in \{0, 1\}, \quad (1a)$$

$$\text{subject to } W_0(\mathbf{x}) = \sum_{j=0}^{N_0-1} w_j x_j \leq W, \quad (1b)$$

where W is the total weight capacity of a knapsack, N_0 is the number of items available, $\{v_j\}$ are the item values, and $\{w_j\}$ are the item weights.

The BKP defined in Eq. (1) involves optimization with the soft constraint of maximizing V , and the hard constraint conditioning the total weight to be smaller than W . It is also called the 0-1 knapsack problem, and is known to belong to the NP-hard computational complexity class.⁵²⁻⁵⁴ Many real-world optimization problems can be represented as a BKP,⁵⁵ including optimization tasks for molecular drug discovery.⁵⁶

The constrained optimization of Eq. (1) can be transformed to an unconstrained problem by introducing auxiliary binary variables $\{y_j\}$ to have a QUBO representation.^{49,50}

$$\min_{\mathbf{x}, \mathbf{y}} E = -V(\mathbf{x}) + \lambda \left[W - W_0(\mathbf{x}) - \sum_{j=0}^{N_1-1} 2^j y_j \right]^2, \quad (2)$$

where λ is the quadratic penalty weight and the sum of $N_1 = \lceil \log_2(W+1) \rceil$ terms. We can now write the cost function $E(\mathbf{x})$ as a function of $N_0 + N_1$ binary variables $\{x_j\}$, including the auxiliary variables:

$$\begin{aligned} \min_{\mathbf{x}} E = & - \sum_{j=0}^{N_0-1} v_j x_j + \lambda \left[W - \sum_{j=0}^{N_0-1} w_j x_j \right. \\ & \left. - \sum_{j=N_0}^{N_0+N_1-1} 2^{j-N_0} x_j \right]^2. \end{aligned} \quad (3)$$

This cost function can now be mapped to a qubit Hamiltonian H_Q of $N = N_0 + N_1$ qubits by substituting each binary variable, as follows: $x_j \mapsto \frac{1}{2}(\mathbb{I}_j - Z_j)$, where \mathbb{I} and Z are the identity and Pauli-Z operators, while the subscript index represents the qubit site. The mapping from binary variable to qubit operator can be easily justified by noting that the eigenstates of the Z operator are the qubit basis states $|0\rangle$ and $|1\rangle$ with eigenvalues $+1$ and -1 , respectively. The multi-qubit Hamiltonian can then be written, as follows:

$$\begin{aligned} H_Q = & - \sum_{j=0}^{N_0-1} \frac{v_j}{2} (\mathbb{I}_j - Z_j) + \lambda \left[W - \sum_{j=0}^{N_0-1} \frac{w_j}{2} (\mathbb{I}_j - Z_j) \right. \\ & \left. - \sum_{j=N_0}^{N_0+N_1-1} 2^{j-N_0-1} (\mathbb{I}_j - Z_j) \right]^2. \end{aligned} \quad (4)$$

The binary string \mathbf{x}^* representing the optimal solution of Eq. (3) is now encoded into a tensor product of N computational basis states

$$|\psi\rangle = |x_0^*\rangle \otimes \cdots \otimes |x_{N-1}^*\rangle, \quad (5)$$

and is the ground state of H_Q . Similar to the BKP problem discussed above, any constrained optimization problem can be represented by a Hamiltonian H_Q of the form defined in Eq. (4) by representing the constraints by auxiliary variables and designing a quadratic penalty function.

B. Hilbert space mapping

Let us define a N -qubit Hamiltonian H_D below that can be written as a linear combination of terms, each consisting of only identity and Pauli-Z operators

$$H_D = \sum_{\mu=1}^{N_H} g_{\mu} \sigma_1^{(\mu)} \otimes \cdots \otimes \sigma_N^{(\mu)} = \sum_{\mu=1}^{N_H} g_{\mu} \mathcal{D}_N^{(\mu)}, \quad (6)$$

where $\sigma_j = \mathbb{I}, Z$, the Hamiltonian coefficients $\{g_{\mu}\}$ are known, and the number of terms N_H is assumed to be a computationally manageable finite number. For example, H_Q defined in Eq. (4) consists of $\mathcal{O}(N_0^2 + N_1^2 + N_0 N_1)$ terms. Each of the $\mathcal{D}_N^{(\mu)}$ terms is a diagonal operator since

$$\mathbb{I} = |0\rangle\langle 0| + |1\rangle\langle 1|, \quad (7a)$$

$$Z = |0\rangle\langle 0| - |1\rangle\langle 1|. \quad (7b)$$

Our goal is to compute $\langle \psi | \mathcal{D}_N^{(\mu)} | \psi \rangle$ for a given state using a combination of Pauli-Z measurements on a qubit and photon number measurements on qumodes. The photon number measurements compute the probabilities of finding the discrete Fock states $\{|n\rangle\}_{n \in \mathbb{N}}$ of a quantum harmonic oscillator or the number of photons in an optical mode, and are the eigenstates of the bosonic number operator, $\hat{n} |n\rangle = \hat{a}^\dagger \hat{a} |n\rangle = n |n\rangle$, where \hat{a}^\dagger, \hat{a} are bosonic creation and annihilation operators, respectively. For a realistic setup, the maximum number of photons can be set to a finite integer $L - 1$, where L is called the Fock cutoff. From the Fock basis perspective, a qumode is thus equivalent to a multilevel generalization of a qubit in L dimensions, also known as a qudit.⁵⁷

Let us first discuss the computation of the expectation values in the context of photon number measurements of one qumode for the sake of simplicity. The observable $\langle \psi | \mathcal{D}_N^{(\mu)} | \psi \rangle$ can be computed from the histogram of all possible binary strings $|q_1, \dots, q_N\rangle_Q$ from Pauli-Z measurements since

$$\langle \psi | Z_{p_1} \cdots Z_{p_N} | \psi \rangle = \sum_{\mathbf{b}} (-1)^{\sum_{i=1}^N b_{p_i}} \mathbb{P}(\mathbf{b}), \quad (8)$$

where $\{\mathbf{b}\}$ represent all qubit basis states as bitstrings, $\mathbb{P}(\mathbf{b})$ is the probability of measuring the state $|\mathbf{b}\rangle$ and

$\sum_{i=1}^N b_{p_i}$ is the sum of the bit values at positions $\{p_1, \dots, p_N\}$, which determines the sign for each qubit in the Pauli word. Each of the binary bitstrings of N qubits can be in principle mapped to the Fock space of a single qumode with $L = 2^N$ using the binary mapping

$$|q_1, \dots, q_N\rangle_Q \leftrightarrow |n\rangle_B, \quad (9)$$

where $n = 2^0 q_1 + \dots + 2^{N-1} q_N$. Thus, the histogram of binary strings can be generated by photon number measurements on a single qumode instead of Pauli-Z measurements on multiple qubits. A single qumode Hilbert space with a realistic cutoff L can only handle mapping a few qubits realistically. However, we can expand the Hilbert space significantly by working with multiple qumodes, thus allowing the mapping of a large number of qubits with fewer qumodes by a constant factor $\log_2(L)$. In this work, we will focus on a hardware setup with one qubit and two qumodes, which can be readily generalized to multiple qumodes. Thus, we will explore partitioning the N -qubit Hilbert space such that it matches with the combined Hilbert space of one qubit and two qumodes, i.e., $2^N = 2 \times L_1 \times L_2$, where L_1 and L_2 are the Fock cutoffs for the first and second qumodes, respectively. Thus, the N -qubit state $|q_1, \dots, q_N\rangle_Q$ Hilbert space can now be partitioned into three pieces and mapped to

$$\begin{aligned} & |q_1\rangle_Q \otimes |q_2, \dots, q_{N-j}\rangle_Q \otimes |q_{N-j+1}, \dots, q_N\rangle_Q \\ & \leftrightarrow |q_1\rangle_Q \otimes |n\rangle_B \otimes |m\rangle_B, \end{aligned} \quad (10)$$

where $1 \leq j \leq N-2$. For example, one possible partition for the Hamiltonian H_Q defined in Eq. (4) can be that the N_0 primary variables are represented by the qubit and the first qumode, whereas the second qumode represents the N_1 auxiliary variables. Let us discuss with a simple example where a one-qubit two-qumode quantum state $|\psi\rangle$ is prepared, followed by Pauli-Z measurement on the qubit and photon number measurements on the two qumodes. Let us also assume $|\psi\rangle$ is originally representing a five-qubit Hamiltonian, which has been partitioned such that the first qubit remains the same, where the rest of the four qubits are grouped into two equal parts and each mapped to one qumode. The measured bitstrings of the first subsystem remain the same, i.e., $|0\rangle$ and $|1\rangle$. For each of the second and third subsystems, the possible bitstrings can be mapped as

$$|0\rangle \otimes |0\rangle_Q \leftrightarrow |0\rangle_B, \quad |0\rangle \otimes |1\rangle_Q \leftrightarrow |1\rangle_B, \quad (11a)$$

$$|1\rangle \otimes |0\rangle_Q \leftrightarrow |2\rangle_B, \quad |1\rangle \otimes |1\rangle_Q \leftrightarrow |3\rangle_B. \quad (11b)$$

For example, the one-qubit two-qumode basis state $|1\rangle_Q \otimes |3\rangle_B \otimes |2\rangle_B$ is same as the five-qubit basis state $|1, 1, 1, 1, 0\rangle_Q$.

A novel characteristic of our approach is the use of photon number measurements to output positive integers that can be easily converted to binary strings for evaluating the expectation value of the qubit-based Hamiltonian H_Q as defined in Eq. (6) or H_D of Eq. (4). Photon number measurements can be implemented using the

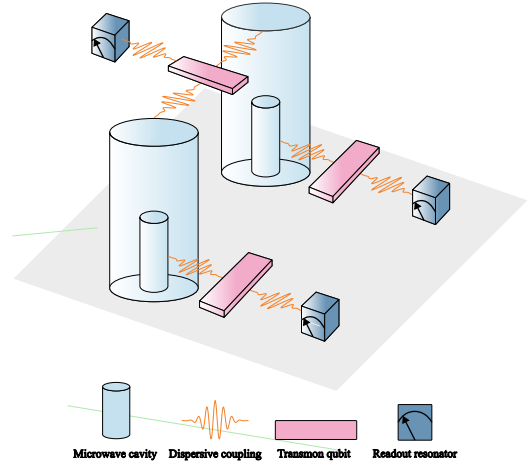


FIG. 2. Schematic to implement quantum nondemolition (QND) approach for photon number measurements for two qumodes with computational measurements for the coupled qubit. Two microwave cavities are dispersively coupled to a coupler transmon qubit with a readout resonator for computational basis measurement of the coupler qubit. Each of the cavities are also coupled to an ancillary transmon qubit with a readout resonator which allows for photon number detection followed by the approach discussed in Ref. 44.

quantum nondemolition (QND) method, as described in Ref. 44. The QND measurement relies on the dispersive coupling between the cavity mode and its ancillary transmon qubit. In the dispersive regime, the transition frequency of the transmon qubit shifts depending on the photon number in the cavity. This shift enables the transmon to encode information about the cavity's photon state. A sequence of numerically optimized control pulses is applied to the transmon to extract this information. These pulses selectively drive the transmon between its quantum states based on the binary representation of the photon number. The transmon state carrying photon number information is probed via a dispersive readout. This QND scheme achieves high resolution and fidelity, resolving photon numbers up to 15 in single-shot experiments.⁴⁴ We refer the reader to Figure 2 for a schematic of the hardware setup where photon number measurements on two qumodes is combined with computational basis measurements on a qubit.

While computing the expectation values of the Hamiltonian in binary basis is a generally effective strategy, we may also rewrite the auxiliary binary variables $\{y_j\}$ in Eq. (2) in the basis of the photon number cutoff L of the qubits. As an example, we can use one integer variable b ,

$$\min_{\mathbf{x}, \mathbf{y}} E = -V(\mathbf{x}) + \lambda \left[W - W_0(\mathbf{x}) - b \right]^2, \quad (12)$$

such that it has values $b = 0, \dots, 2^{N_1} - 1$. By representing

the integer variable to the bosonic number operator $b \mapsto \hat{n}$, we can now map the qubit Hamiltonian H_Q defined in Eq. (4) to a qubit-qumode Hamiltonian of the form

$$H_Q \mapsto H_{QB} = - \sum_{j=0}^{N_0-1} \frac{v_j}{2} (\mathbb{I}_j - Z_j) + \lambda \left[W - \sum_{j=0}^{N_0-1} \frac{w_j}{2} (\mathbb{I}_j - Z_j) - \hat{n} \right]^2, \quad (13)$$

where the number operator \hat{n} is assumed to have the Fock cutoff $L = 2^{N_1} - 1$ and the corresponding qumode represents all of the auxiliary variables. This ensures that the photon number measurements corresponding to the Hilbert space of the auxiliary variables can be used directly without the integer-to-binary mapping, and to fewer Hamiltonian terms compared to the qubit-only Hamiltonian defined in Eq. (4).

Finally, it is also possible to represent and evaluate the Hamiltonian directly in the basis of the experimental qubit-qumode device in the projection operator form

$$H_Q \mapsto H_B = \sum_{i \in \{Q, B1, B2\}} \sum_{n=0}^{L_i} C_n^i \mathbb{P}_n^{(i)} + \sum_{i, j \in \{Q, B1, B2\}} \sum_{n=0}^{L_i} \sum_{m=0}^{L_j} C_{n,m}^{i,j} \mathbb{P}_n^{(i)} \otimes \mathbb{P}_m^{(j)} \quad (14)$$

where $\mathbb{P}_n^{(i)} \equiv |n\rangle \langle n|$ is defined in the Hilbert space of the qubit mode ($i = Q$) of dimension 2 or the bosonic modes ($i = B_1$ or B_2) of dimension L_1 or L_2 . $\{C_n^i\}$ and $\{C_{n,m}^{i,j}\}$ can be deduced by rewriting the single- or two-qubit Pauli Z operators in the qubit Hamiltonian Eq. (4) following the qubit-to-qumode mapping. For example, given the mapping Eq. (11), we have $Z_2 Z_3 = |0\rangle \langle 0| - |1\rangle \langle 1| - |2\rangle \langle 2| + |3\rangle \langle 3|$. We note that for a large problem with many qubits and qumodes, the number of terms in the Hamiltonian will only grow quadratically with the number of modes.

C. Variational quantum eigensolver

We take a variational quantum eigensolver (VQE) approach to find the approximate ground state of the diagonal Hamiltonian H_D defined in Eq. (6) by optimizing the following cost function

$$\min_{\psi} E = \langle \psi | H_D | \psi \rangle = \sum_{\mu=1}^{N_H} g_{\mu} \langle \psi | \mathcal{D}_N^{(\mu)} | \psi \rangle, \quad (15)$$

where $\mathcal{D}_N^{(\mu)}$ can be computed using a qubit-qumode device following the steps below.

- Prepare a normalized trial one-qubit two-qumode state $|\psi\rangle$ using a parameterized quantum circuit.

- Generate the histogram of $|q\rangle_Q \otimes |n\rangle_B \otimes |m\rangle_B$ using Pauli-Z measurements on the qubit and photon number measurements on the two qumodes.⁴⁴

- Compute the expectation value by combining Eq. (8) and Eq. (10).

The trial state $|\psi\rangle$ can be generated by a parameterized one-qubit two-qumode circuit acting on the vacuum state

$$|\psi(\mathbf{v})\rangle = U(\mathbf{v}) (|0\rangle_Q \otimes |0\rangle_C \otimes |0\rangle_C), \quad (16)$$

where the vector \mathbf{v} represents all the circuit parameters. The parameters can be updated by optimizing Eq. (15) on a classical computer. The histograms on the qubit-qumode device compute the following probabilities

$$S_{q,n,m} = |\langle q, n, m | \psi \rangle|^2, \quad (17)$$

where $q = \{0, 1\}$, $n = \{0, 1, \dots, L_1 - 1\}$, and $m = \{0, 1, \dots, L_2 - 1\}$ are the possible basis states. After repeating the measurement experiments for a finite number of times, a distribution for $\{S_{q,n,m}\}$ can be generated for computing the expectation values.

The overlaps $\{S_{q,n,m}\}$ also measure how close the approximate ground state $|\psi\rangle$ — a state in a superposition of multiple solution strings — is to the optimal solution string. Thus, for the QUBO problems, we only care about the resolution of the distribution generated by the measurements $\{S_{q,n,m}\}$ instead of how close the trial energy E is to the true ground state energy of the Hamiltonian H_D . The quantum superposition of $|\psi\rangle$ also highlights the potential advantage of quantum optimization algorithms. The parameterized one-qubit two-qumode trial state can be generically represented as

$$|\psi(\mathbf{v})\rangle = \sum_{q \in \{0, 1\}} \sum_{n=0}^{L_1-1} \sum_{m=0}^{L_2-1} \lambda_{q,n,m}(\mathbf{v}) |q, n, m\rangle, \quad (18)$$

and the optimization steps depend on the gradient for the cost function defined in Eq. (15)

$$\frac{\partial E}{\partial \mathbf{v}} = \langle \frac{\partial \psi}{\partial \mathbf{v}} | H_D | \psi \rangle + \langle \psi | H_D | \frac{\partial \psi}{\partial \mathbf{v}} \rangle, \quad (19)$$

which in turn updates $|\psi(\mathbf{v})\rangle$ for the next iteration based on Eq. (16). This means that at each optimization step, all the combinatorial number of basis state coefficients affect the variational parameters, which in turn update all the basis state coefficients at the same time in the next iteration. This can be hard to mimic using a classical distribution that only samples from a subspace of the full Hilbert space.^{58–60} Nevertheless, the true potential of quantum superposition is achieved when the parameterized circuit for $|\psi(\mathbf{v})\rangle$ is sufficiently expressive, which we discuss below in the context of qubit-controlled bosonic qumode gates.

The parameterized circuit for the trial state defined in Eq. (16) must be a universal ansatz for the one qubit

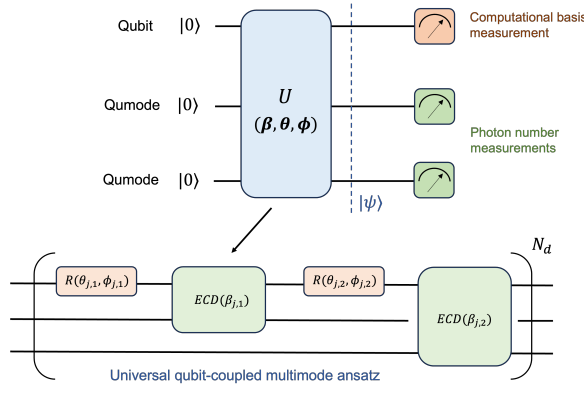


FIG. 3. Hybrid one-qubit two-qumode circuit followed by measurements for computation of expectation values of a diagonal Hamiltonian as defined in Eq. (6). The circuit consists of echoed conditional displacement (ECD) qubit-qumode gates with one-qubit rotations, as discussed in Section II C.

and multiple qumodes, which can be achieved in multiple ways.^{38,40–42,61} We explore a universal ansatz based on the following circuit here⁴¹

$$U(\mathbf{v}) = U_{ER}(\beta_{N_d}, \theta_{N_d}, \phi_{N_d}) \cdots U_{ER}(\beta_1, \theta_1, \phi_1). \quad (20)$$

The building block unitaries U_{ER} are built from one-qubit arbitrary rotations

$$R(\theta, \phi) = e^{-i(\theta/2)[\cos(\phi)X + \sin(\phi)Y]}, \quad (21)$$

and two one-qubit one-qumode echoed conditional displacement (ECD) operations³⁹

$$U_{ER}(\beta_j, \theta_j, \phi_j) = ECD_{0,2}(\beta_{j,2}) R_0(\theta_{j,2}, \phi_{j,2}) \times ECD_{0,1}(\beta_{j,1}) R_0(\theta_{j,1}, \phi_{j,1}), \quad (22a)$$

$$ECD_{0,1}(\beta_1) = \sigma_0^- D_1(\beta_1/2) + \sigma_0^+ D_1(-\beta_1/2), \quad (22b)$$

$$ECD_{0,2}(\beta_2) = \sigma_0^- D_2(\beta_2/2) + \sigma_0^+ D_2(-\beta_2/2), \quad (22c)$$

where $D(\beta) = e^{\beta\hat{a}^\dagger - \beta^*\hat{a}}$ is the qumode displacement operator, X, Y are Pauli matrices, and $\sigma^+ = |0\rangle\langle 1|, \sigma^- = |1\rangle\langle 0|$ are the qubit transition operators. The operator subscripts in Eq. (22) represent the indexing for the qubit and the two qumodes, and tensor product is assumed. Other choices for universal ansatz include selective number-dependent arbitrary phase (SNAP) with displacement and beamsplitters,^{38,43} and conditional-not displacement gates.⁴⁰ The variables $\{\beta, \theta, \phi\}$ in Eq. (20) are matrices of dimensions $N_d \times 2$, where the complex-valued β matrix can also be split into two real-valued matrices of same dimensions such that $\beta_{j,k} = r_{j,k} e^{i\phi_{j,k}}$ for each complex-valued element. We call the number of blocks N_d in Eq. (20) as the depth of the universal ECD-rotation circuit. Thus, the packed vector \mathbf{v} representing all the real-valued parameters has $8N_d$ dimensions. The full circuit is illustrated in Figure 3.

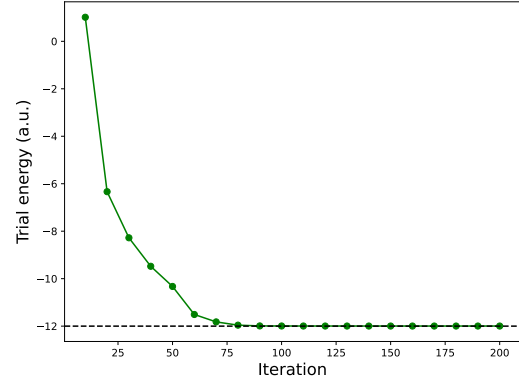


FIG. 4. Trial energy values defined in Eq. (15) at different ECD-VQE iterations while finding the ground state of H_Q defined in Eq. (25). The horizontal black line represents the exact ground state energy. The circuit depth for the trial state is $N_d = 5$.

III. APPLICATIONS

We now have all the tools needed to implement the ECD-VQE method for finding the ground state of a diagonal H_B . We show the applications of our ECD-VQE approach with two specific examples here.

A. Binary knapsack problem

Let us discuss a simple binary knapsack problem. Let us assume we have $N_0 = 4$ items with their values and weight constraints given by

$$\max_{\mathbf{x}} 2x_0 + 5x_1 + 7x_2 + 3x_3, \quad (23a)$$

$$\text{subject to } 2.5x_0 + 3x_1 + 4x_2 + 3.5x_3 \leq 7. \quad (23b)$$

Following the discussions in Section II A, the above optimization can be recast as the following QUBO problem

$$\begin{aligned} \min_{\mathbf{x}} E = & -(2x_0 + 5x_1 + 7x_2 + 3x_3) \\ & + \lambda \left[7 - (2.5x_0 + 3x_1 + 4x_2 + 3.5x_3) \right. \\ & \left. - (x_4 + 2x_5 + 4x_6) \right]^2 \end{aligned} \quad (24)$$

consisting of $4 + 3 = 7$ binary variables. For the penalty weight $\lambda = 2$, the corresponding seven-qubit Hamiltonian

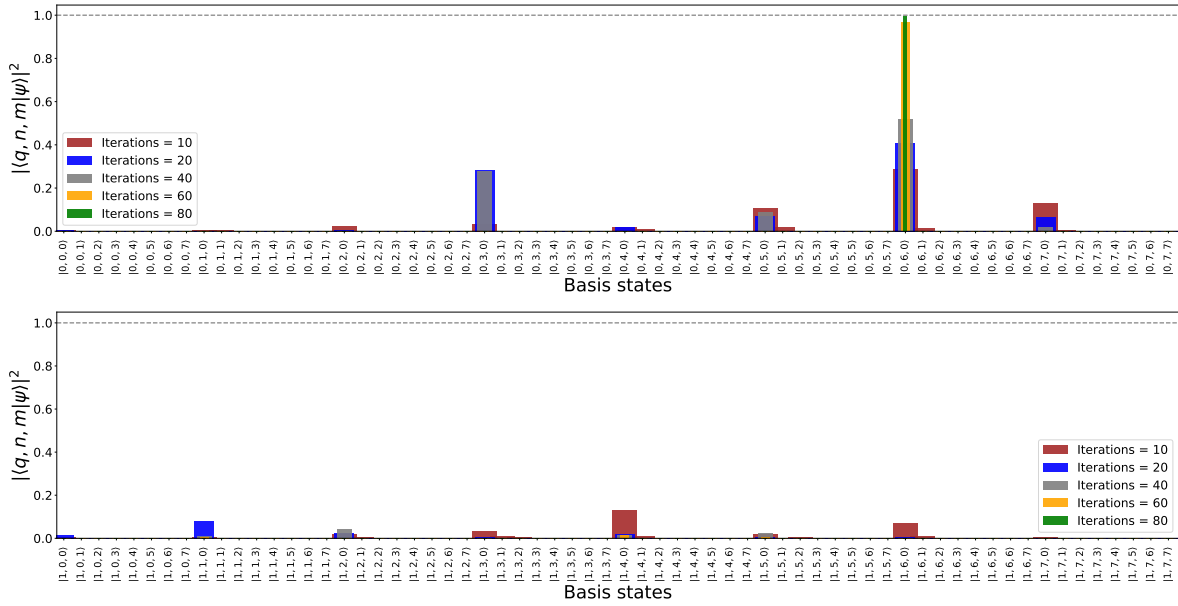


FIG. 5. Probabilities $S_{q,n,m} = |\langle q, n, m | \psi \rangle|^2$ at different numbers of iterations of the ECD-VQE method for the one-qubit two-qumode Hamiltonian H_Q defined in Eq. (25). The histograms are split into two parts for better readability of the basis states. The circuit depth for the trial state is $N_d = 5$. The corresponding trial energy values are shown in Figure 4.

is given by

$$\begin{aligned}
 H_Q = & 41.75 - 14.0 Z_0 - 15.5 Z_1 - 20.5 Z_2 - 19.5 Z_3 \\
 & - 6.0 Z_4 - 12.0 Z_5 - 24.0 Z_6 + 7.5 Z_0 Z_1 + 10.0 Z_0 Z_2 \\
 & + 8.75 Z_0 Z_3 + 2.5 Z_0 Z_4 + 5.0 Z_0 Z_5 + 10.0 Z_0 Z_6 \\
 & + 12.0 Z_1 Z_2 + 10.5 Z_1 Z_3 + 3.0 Z_1 Z_4 + 6.0 Z_1 Z_5 \\
 & + 12.0 Z_1 Z_6 + 14.0 Z_2 Z_3 + 4.0 Z_2 Z_4 + 8.0 Z_2 Z_5 \\
 & + 16.0 Z_2 Z_6 + 3.5 Z_3 Z_4 + 7.0 Z_3 Z_5 + 14.0 Z_3 Z_6 \\
 & + 2.0 Z_4 Z_5 + 4.0 Z_4 Z_6 + 8.0 Z_5 Z_6. \quad (25)
 \end{aligned}$$

Qumode-based ECD-VQE: The ground state of H_Q obtained by exact diagonalization is $|0, 1, 1, 0\rangle_Q \otimes |0, 0, 0\rangle_Q$ with eigenvalue -12. Indeed, the optimal solution is $\mathbf{x}^* = (0, 1, 1, 0)$ with the corresponding weight = 7 and value = 12. We will now partition the seven-qubit Hamiltonian into three parts such that it will be mapped to a one-qubit two-qumode system with the Fock cutoff for each qumode being $L = 8$. In other words, we map the first four qubits corresponding to the primary variables to the qubit along with the first qumode, and the rest to the second qumode. The ground state of H_Q is now mapped as

$$|0, 1, 1, 0\rangle_Q \otimes |0, 0, 0\rangle_Q \leftrightarrow |0\rangle_Q \otimes |6\rangle_C \otimes |0\rangle_C, \quad (26)$$

or in shorthand, $|0, 6, 0\rangle$. This is the solution state that we seek with this model benchmark system.

We show the trial energies for the ECD-VQE method applied to H_Q of Eq. (25) in Figure 4. The circuit

depth chosen for the trial state is $N_d = 5$. We emulated the expectation values classically using the QuTiP Python library⁶² and optimized the energy function of Eq. (15) using the Broyden–Fletcher–Goldfarb–Shanno (BFGS) algorithm as implemented in the SciPy Python library.⁶³ It is clear from Figure 4 that the ECD-VQE method discussed here practically converges to the exact ground state energy in approximately 100 iterations. The goal in traditional VQE approaches is usually to find highly accurate ground state energies, whereas our goal

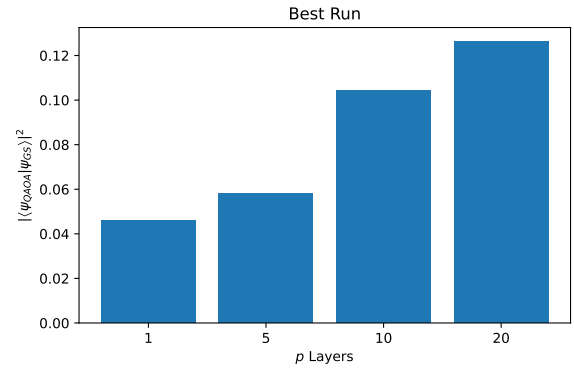


FIG. 6. Optimal probabilities for different numbers of QAOA layers chosen out of 50 independent trials for the ground state of the seven-qubit Hamiltonian defined in Eq. (25). Each trial converged with ~ 150 iterations with the classical optimizer.

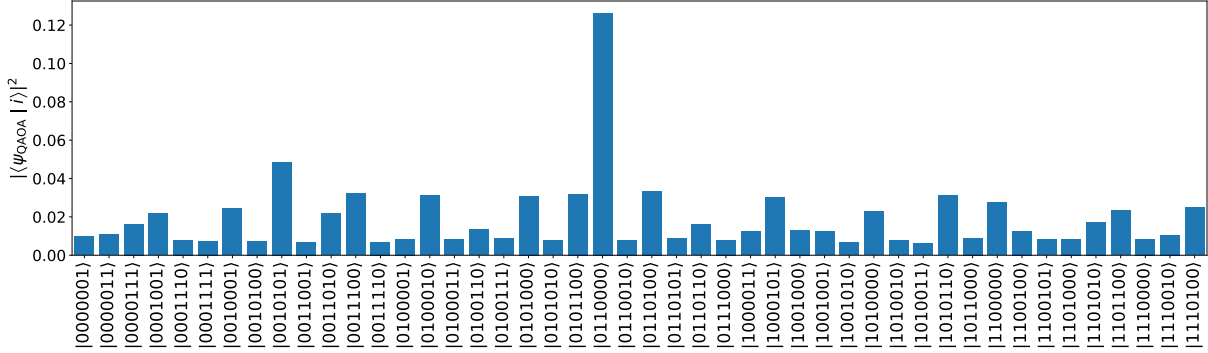


FIG. 7. Measurement probabilities for bitstring basis states for the optimal QAOA state with $p = 20$ -layers for the seven-qubit Hamiltonian defined in Eq. (25).

here is to resolve the ground state $|0, 6, 0\rangle$, which represents the optimal solution. We plot the corresponding $\{S_{q,n,m}\}$ probability values as defined in Eq. (17) during different iterations of ECD-VQE in Figure 5. The ground state is practically resolved after 80 iterations and emerges as the highest peak even in 10 iterations, as shown in Figure 5. Thus, resolving the ground state may be achieved using a relatively smaller number of classical optimization steps than for finding the energy. We highlight that the $\{S_{q,n,m}\}$ probability values are directly available from photon number and Pauli-Z measurement histograms without the need for explicitly iterating over all possible integer strings, such as in a classical simulator.

Qubit-based ECD-VQE: Implementing the ECD-VQE ansatz on a qubit-only device would result in extremely deep circuits,^{43,44} motivating our use of hybrid qubit-qumode hardware. To estimate the equivalent qubit-only resource cost, we transpile the qubit-qumode unitaries using Qiskit,⁶⁴ employing Pauli rotations and CNOT gates as the elementary operations. For this problem, with a Fock cutoff $L = 8$ per qumode, each qumode becomes encoded using four qubits, including an ancilla. Transpilation shows that a single ECD gate maps to 93 CNOT gates and yields a circuit depth of approximately 270 on a four-qubit register. Consequently, the ECD-rotation ansatz with $N_d = 5$ blocks, mentioned above, comprising 10 ECD gates, corresponds to a total of 930 CNOT gates in the qubit-only model. Alternatively, compiling the full ansatz (with $N_d = 5$) into a single unitary acting on $N = 7$ qubits results in 7660 CNOT gates and a circuit depth of around 21400. These results highlight that qubit-qumode implementations can achieve comparable expressivity with significantly reduced circuit depth relative to its qubit counterparts.

Qubit-based QAOA: Here, we compare our optimization results for the BKP problem to those obtained using the Quantum Approximate Optimization Algorithm (QAOA) implemented with standard qubit-based circuit^{14,15}. The QAOA implementation is a qubit-only

VQA commonly used as a benchmark for combinatorial binary optimization problems. QAOA can be thought of as a special case of VQE, where the PQC ansatz consists of the alternating application of p -layers of parametrized “mixing” and “problem” unitaries, applied to a quantum register initialized in a uniform superposition

$$|\psi(\beta, \gamma)\rangle = e^{-i\beta_p H_M} e^{-i\gamma_p H_P} \dots e^{-i\beta_2 H_M} e^{-i\gamma_2 H_P} e^{-i\beta_1 H_M} e^{-i\gamma_1 H_P} |+\rangle^{\otimes N}. \quad (27)$$

The problem Hamiltonian H_P in this case is same as in Eq. (25), whereas the mixing Hamiltonian is defined as

$$H_M = \sum_{j=0}^{N-1} \sigma_j^x. \quad (28)$$

The QAOA calculations were implemented numerically with QuTiP using the BFGS classical optimizer.

The optimal QAOA result out of 50 independent trials for increasing layers is shown in Figure 6. These results show that the probability of measuring the bitstring corresponding to the solution generally increases by increasing the number of layers. We note that the QAOA approach with $p = 20$ layers has the same number of variational parameters as the ECD-VQE approach with $N_d = 5$ blocks, highlighting the more favorable optimization landscape for the ECD-based approach. We also note that the number of CNOT gates per layer scales as $\mathcal{O}(N^2)$ for QUBO problems where N is the number of qubits⁶⁵. Indeed, the number of two-qubit CNOT gates needed for the BKP problem discussed here for only one layer is 42, which is more than the gate counts for the ECD-VQE approach, where $N_d = 5$ blocks correspond to only 10 one-qubit one-qumode ECD gates.

Since the highest probability of measuring the solution was obtained with $p = 20$ layers, we chose to sample the measurement outcomes with this optimal QAOA circuit. The results of the measurement sampling are shown in Figure 7. Although the solution bitstring has the highest measurement probability, we see that there is still a substantial likelihood of sampling sub-optimal states. The

comparison between Figure 5 and Figure 7 indicates the potential advantages of an expressive VQE ansatz over the QAOA approach, whose ansatz is limited by its cost and mixing Hamiltonians. In our case, the VQE ansatz is provided by a set of native qubit-qumode gates that reveal the optimal solutions with the help of a few blocks of gates.

B. Multiple constraints

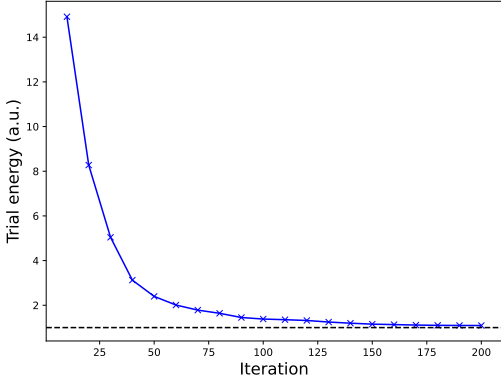


FIG. 8. Trial energy values defined in Eq. (15) at different ECD-VQE iterations while finding the ground state of H_Q defined in Eq. (31). The horizontal black line represents the exact ground state energy. The circuit depth for the trial state is $N_d = 10$.

Our approach can be applied to any constrained optimization problem beyond the BKP problem discussed above. Indeed, let us discuss another simple constrained optimization problem given below

$$\min_{\mathbf{x}} \quad x_0 + 2x_1 + x_2, \quad (29a)$$

$$\text{subject to} \quad x_0 + x_1 = 1, \quad (29b)$$

$$2x_0 + 2x_1 + x_2 \leq 3, \quad (29c)$$

$$x_0 + x_1 + x_2 \geq 1. \quad (29d)$$

which can be represented as the following QUBO problem

$$\begin{aligned} \min_{\mathbf{x}} F = & x_0 + x_1 + x_2 + \lambda_1 (1 - x_0 - x_1)^2 \\ & + \lambda_2 [3 - (2x_0 + 2x_1 + x_2) - (x_3 + 2x_4)]^2 \\ & + \lambda_3 [(x_0 + x_1 + x_2) - x_5 - 1]^2, \end{aligned} \quad (30)$$

consisting of $3 + 3 = 6$ binary variables. For the penalty weight $\lambda = 5$, the corresponding six-qubit Hamiltonian

is given by

$$\begin{aligned} H_Q = & 32.0 - 10.5 Z_0 - 11.0 Z_1 - 5.5 Z_2 - 5.0 Z_3 \\ & - 10.0 Z_4 + 15.0 Z_0 Z_1 + 7.5 Z_0 Z_2 + 5.0 Z_0 Z_3 \\ & + 10.0 Z_0 Z_4 - 2.5 Z_0 Z_5 + 7.5 Z_1 Z_2 + 5.0 Z_1 Z_3 \\ & + 10.0 Z_1 Z_4 - 2.5 Z_1 Z_5 + 2.5 Z_2 Z_3 + 5.0 Z_2 Z_4 \\ & - 2.5 Z_2 Z_5 + 5.0 Z_3 Z_4. \end{aligned} \quad (31)$$

The ground state of H_Q obtained by exact diagonalization is $|1, 0, 0\rangle_Q \otimes |1, 0, 0\rangle_Q$ with eigenvalue 1. Indeed, the optimal solution is $\mathbf{x}^* = (1, 0, 0)$. Let us now reorganize the Hilbert space of the six-qubit Hamiltonian into three parts such that it will be mapped to a one-qubit two-qumode system with the Fock cutoffs for the two qumodes being $L_1 = 4$ and $L_2 = 8$. In other words, we map the first three qubits corresponding to the primary variables to the qubit along with the first qumode, and the rest to the second qumode. The ground state of H_Q is now mapped as

$$|1, 0, 0\rangle_Q \otimes |1, 0, 0\rangle_Q \leftrightarrow |1\rangle_Q \otimes |0\rangle_C \otimes |4\rangle_C, \quad (32)$$

or in shorthand, $|1, 0, 4\rangle$ will be our target state for the ECD-VQE approach as before.

We show the trial energies for the ECD-VQE method applied to H_B of Eq. (31) in Figure 8 and the corresponding overlaps in Figure 9. The circuit depth chosen for the trial state is $N_d = 10$. It is clear that the ground state of the Hamiltonian is fairly resolved after 40 iterations and emerges as the highest peak even in 20 iterations, as shown in Figure 9, even though there is space for the trial energy to converge to lower values even after 200 iterations. This again shows the efficiency of this method in resolving the optimal solution state with just a few optimization iterations.

IV. EFFECTS OF QUMODE NOISE

The implementations of the qumode circuits, followed by photon number measurements discussed in this work, are affected by noise in a realistic hardware setup. The dominant noise source for microwave resonators in cQED is amplitude damping via photon loss, represented by the following rate equation⁴³:

$$\frac{d}{d\tau} \langle \hat{n} \rangle = -\kappa \langle \hat{n} \rangle, \quad (33)$$

where τ is time and κ is the photon loss rate. The transformation of a qumode density matrix ρ due to the amplitude damping quantum channel can be represented by the Kraus operator formalism, as follows:⁶⁶

$$\tilde{\rho} = \sum_{j=0}^{L-1} K_j \rho K_j^\dagger, \quad (34)$$

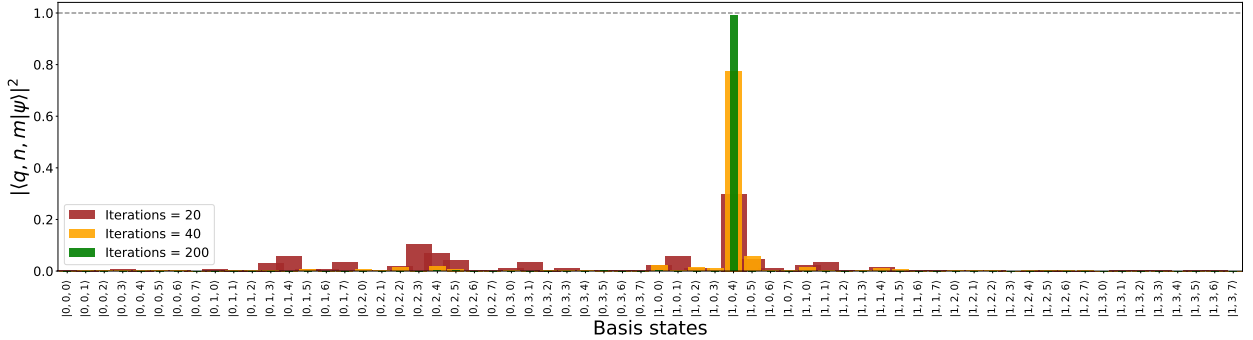


FIG. 9. Probabilities $S_{q,n,m} = |\langle q, n, m | \psi \rangle|^2$ at different numbers of iterations of the ECD-VQE method for the one-qubit two-qumode Hamiltonian H_Q defined in Eq. (31). The circuit depth for the trial state is $N_d = 10$. The corresponding trial energy values are shown in Figure 8.

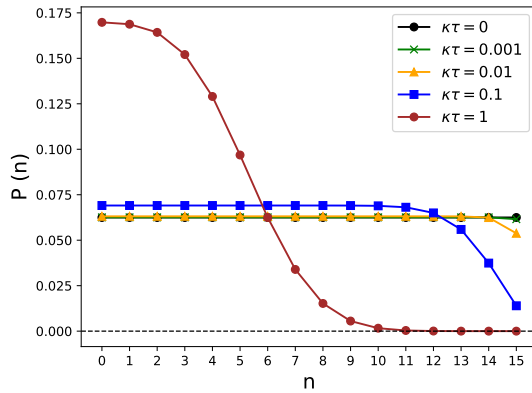


FIG. 10. Effect of amplitude damping as defined in Eq. (35) on the probabilities $P(n)$ of finding the qumode state $|n\rangle$. The initial state ρ is in an equal superposition state with a Fock cutoff of $L = 16$, which then gets modified due to Eq. (34) before simulating the photon number measurements.

where L is the Fock cutoff for the qumode and the Kraus operators are defined, as follows:⁶⁷

$$K_j = \sqrt{\frac{(1 - e^{-\kappa\tau})^j}{j!}} e^{-\frac{\kappa\tau}{2}\hat{n}} \hat{a}^j. \quad (35)$$

Due to the truncated expression of Eq. (34), the K_0 operator must also be modified, as follows:

$$\tilde{K}_0 = \left(\mathbb{I} - \sum_{j=1}^{L-1} K_j^\dagger K_j \right)^{1/2}, \quad (36)$$

so that the transformation remains trace-preserving.⁴³ The modified photon number probabilities for a qumode can now be written as, $P(n) = \text{Tr}(|n\rangle \langle n| \tilde{\rho})$. As an example, we show how amplitude damping, defined according to Eq. (34), affects photon number measurements for an initial qumode state where each Fock basis state has equal amplitudes in Figure 10.

We discuss how photon loss in the qumodes will affect the ECD-VQE optimizations by applying them to the BKP example, discussed in Section III A. The density matrix ρ transformation from the noise channel can be represented as

$$\tilde{\rho} = \sum_{j=0}^{L_1-1} \sum_{k=0}^{L_2-1} (\mathbb{I} \otimes K_j \otimes K_k) \rho (\mathbb{I} \otimes K_j^\dagger \otimes K_k^\dagger), \quad (37)$$

where we have assumed the photon loss rate κ is the same for each of the qumodes and ignored the noise on the qubit. We assume that the noise channels affect the quantum state after each block of ECD with qubit rotation block U_{ER} defined in Eq. (22) is applied, i.e., the time parameter τ in Eq. (35) will be the circuit execution time for each U_{ER} block. After each unitary block is applied, we can represent the updated density matrix as, $\rho \leftarrow U_{ER} \rho U_{ER}^\dagger$, which then undergoes the noise channel transformation as defined in Eq. (37). We show the effects of photon loss on the ECD-VQE optimization for the BKP problem in Eq. (25) in Figure 11, where we plotted the photon number probabilities after 80 iterations. For the noiseless case, 80 iterations are enough to get a resolved peak, as shown in Figure 5. This is also the case up to $\kappa\tau = 0.01$, where the optimization can also resolve the correct solution $|0, 6, 0\rangle$ with certainty. However, the optimization performance starts to deteriorate around $\kappa\tau = 0.1$. Thus, Figure 11 gives us an estimate of how the photon loss rate must relate to the implementation time for qubit-qumode on a real quantum device, which is represented by the $\kappa\tau < 0.1$ regime.

V. DISCUSSION

We have demonstrated the capabilities of ECD-VQE as applied to solving optimization problems with soft and hard constraints, using a qubit-qumode quantum hardware available in cQED devices. We have shown that hardware efficiency could be achieved by using only

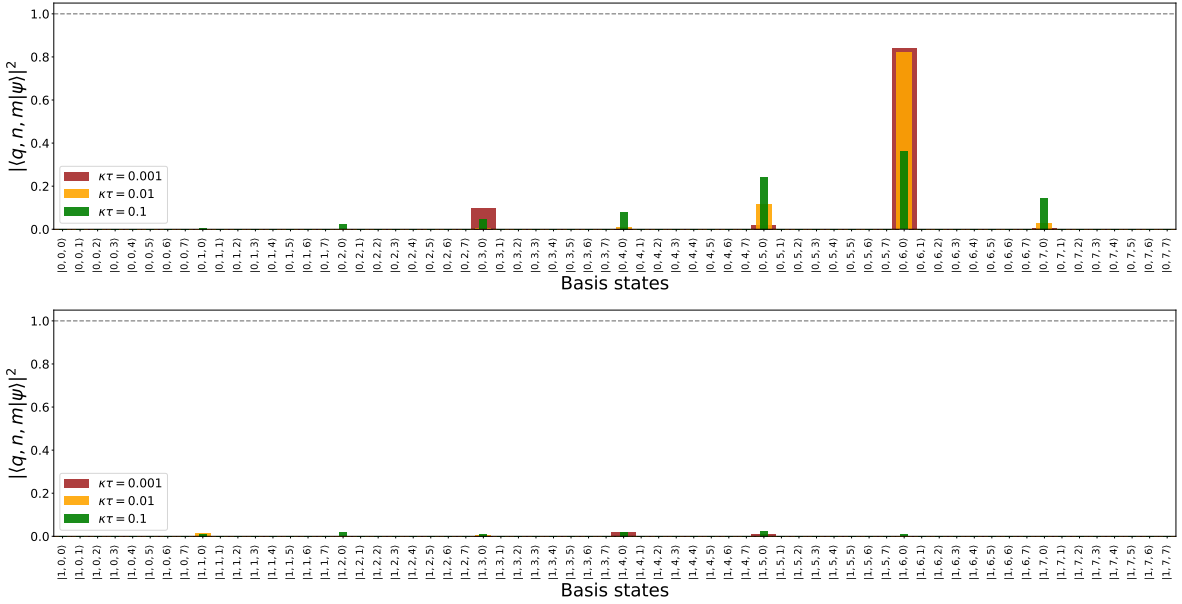


FIG. 11. Effect of qumode amplitude damping as defined in Eq. (37) on the photon number probabilities during the ECD-VQE optimization for the BKP problem defined in Eq. (25). The results are for circuit depth $N_d = 5$ with number of iterations = 80. The histograms are split into two parts for better readability of the basis states. The histograms for different noise parameters $\kappa\tau$ are plotted with different widths for better distinguishability. The corresponding noiseless results are shown in Figure 5.

two qumodes coupled to a single qubit (i.e., two microwave cavities coupled to a transmon qubit). Generalization of our approach to multiple qumodes is straightforward. We have demonstrated our method as applied to a benchmark binary knapsack problem, where seven qubits representing the binary variables of the problem were mapped to one qubit coupled to two qumodes. Furthermore, we have shown how the method can be applied to an optimization problem with multiple constraints corresponding to a six-qubit Hamiltonian.

The ECD-VQE approach requires implementing the qubit-qumode circuit, followed by measuring the state of the qubit and the number of photons in the qumode for computing the expectation values. These measurements are often sufficient to resolve the optimal solution before the cost function value strictly converges to the exact ground state energy. This potentially allows a smaller number of iterations that are needed for resolving the optimal solution relative to traditional VQE, thus allowing ECD-VQE to go beyond the limitations of classical optimization heuristics.⁶⁸ Even with two qumodes, ECD-VQE can be extended to problems with more binary variables based on the Fock cutoff realized by the hardware.

The Hilbert space mapping approach discussed in Section II B can be applied to any multi-qubit Hamiltonian with diagonal terms, i.e., terms involving only Pauli-Z and identity operators. Thus, our approach applies to any QUBO problem that is first mapped into a qubit Hamiltonian before representing it in terms of

the Hilbert space of a composite one-qubit multi-qumode system. Specifically, R number of qumodes coupled to one qubit is equivalent to the number of qubits $N = 1 + \lceil \log_2(\prod_{j=1}^R L_j) \rceil$, where $\{L_j\}$ are the Fock cutoffs for the qumodes. This is a significant resource reduction going from a qubit-centric architecture to the hybrid qubit-qumode approach with the flexibility of increasing the number of qumodes or Fock cutoffs based on the hardware resource, while also allowing significantly shallower circuits compared to qubit-centric architecture because of the expressivity of the ECD gates compared to native qubit gates.

We have mostly focused on implementing the ECD-VQE method with a noiseless simulator to highlight the novelty of this approach. We have discussed the effect of photon loss in the resonator qumode, the dominant noise source in a realistic cQED setup, on the optimization in Section IV. The photon loss rate and ECD gate implementation times are currently on the same timescale.³⁹ The effects of the decoherence associated with the transmon qubit on the resonator qumodes is avoided using weak dispersive coupling between the qubit and the resonator qumodes combined with fast pulses,^{69,70} which has also been shown for the ECD-rotation ansatz.⁴¹

Quantum error correction (QEC) applied to Fock states of qumodes beyond the first two levels can resolve the noise error,^{71–73} which is a challenge for near-term hardware. Nevertheless, huge progress has been recently made in demonstrating error-corrected logical qubits us-

ing qumode resonators beyond break-even,³⁶ and extended for Fock levels of qumodes as well.³⁷ One promising approach with contemporary hardware to tackle the photon loss noise is quantum error mitigation (QEM) techniques, which manage errors on noisy quantum devices. Multiple QEM strategies have been developed for qumode photon loss,^{74–77} and we leave the combination of these approaches with our ECD-VQE method as future work.

ACKNOWLEDGMENTS

The authors acknowledge partial support from the National Science Foundation Engines Development Award:

Advancing Quantum Technologies (CT) under Award Number 2302908. VSB acknowledges partial support from Boehringer Ingelheim and from the NSF Center for Quantum Dynamics on Modular Quantum Devices (CQD-MQD) under grant number 2124511. CW acknowledges partial support from the Department of Energy (Grant No. DE-SC0025521).

CODE AND DATA AVAILABILITY

The Python code and data for the optimizations can be found at https://github.com/CQDMQD/codes_qumode_qubo.

- ¹ J. R. McClean, J. Romero, R. Babbush, and A. Aspuru-Guzik, *New J. Phys.* **18**, 023023 (2016).
- ² M. Cerezo, A. Arrasmith, R. Babbush, S. C. Benjamin, S. Endo, K. Fujii, J. R. McClean, K. Mitarai, X. Yuan, L. Cincio, *et al.*, *Nat. Rev. Phys.* **3**, 625 (2021).
- ³ J. Tilly, H. Chen, S. Cao, D. Picozzi, K. Setia, Y. Li, E. Grant, L. Wossnig, I. Rungger, G. H. Booth, *et al.*, *Phys. Rep.* **986**, 1 (2022).
- ⁴ A. Callison and N. Chancellor, *Phys. Rev. A* **106**, 010101 (2022).
- ⁵ K. Yawata, Y. Osakabe, T. Okuyama, and A. Asahara, in *2022 IEEE International Conference on Big Data (Big Data)* (IEEE, 2022) pp. 2437–2440.
- ⁶ A. Ajagekar and F. You, *npj Comput. Mater.* **9**, 143 (2023).
- ⁷ T. Zaborniak, J. Giraldo, H. Müller, H. Jabbari, and U. Stege, in *2022 IEEE International Conference on Quantum Computing and Engineering (QCE)* (IEEE, 2022) pp. 174–185.
- ⁸ K. Yanagisawa, T. Fujie, K. Takabatake, and Y. Akiyama, *Entropy* **26**, 397 (2024).
- ⁹ P. Date, D. Arthur, and L. Pusey-Nazzaro, *Sci. Rep.* **11**, 10029 (2021).
- ¹⁰ T. Matsumori, M. Taki, and T. Kadowaki, *Sci. Rep.* **12**, 12143 (2022).
- ¹¹ S. Feld, C. Roch, T. Gabor, C. Seidel, F. Neukart, I. Galter, W. Mauerer, and C. Linnhoff-Popien, *Frontiers in ICT* **6**, 13 (2019).
- ¹² D. Laughhunn, *Oper. Res.* **18**, 454 (1970).
- ¹³ A. Peruzzo, J. McClean, P. Shadbolt, M.-H. Yung, X.-Q. Zhou, P. J. Love, A. Aspuru-Guzik, and J. L. O’Brien, *Nat. Commun.* **5**, 4213 (2014).
- ¹⁴ E. Farhi, J. Goldstone, and S. Gutmann, arXiv preprint arXiv:1411.4028 (2014).
- ¹⁵ K. Blekos, D. Brand, A. Ceschini, C.-H. Chou, R.-H. Li, K. Pandya, and A. Summer, *Phys. Rep.* **1068**, 1 (2024).
- ¹⁶ A. G. Taube and R. J. Bartlett, *Int. J. Quantum Chem.* **106**, 3393 (2006).
- ¹⁷ A. Anand, P. Schleich, S. Alperin-Lea, P. W. Jensen, S. Sim, M. Díaz-Tinoco, J. S. Kottmann, M. Degroote, A. F. Izmaylov, and A. Aspuru-Guzik, *Chem. Soc. Rev.* **51**, 1659 (2022).
- ¹⁸ M. Willsch, D. Willsch, F. Jin, H. De Raedt, and K. Michielsen, *Quantum Inf. Process.* **19**, 1 (2020).
- ¹⁹ J. Rajakumar, J. Golden, A. Bärtschi, and S. Eidenbenz, in *Proceedings of the 21st ACM International Conference on Computing Frontiers* (2024) pp. 199–206.
- ²⁰ S. Singhal, V. Srivastava, P. Rohith, P. Jain, and D. Bhowmik, in *2024 8th IEEE Electron Devices Technology & Manufacturing Conference (EDTM)* (IEEE, 2024) pp. 1–3.
- ²¹ T. Müller, A. Singh, F. K. Wilhelm, and T. Bode, arXiv preprint arXiv:2411.19388 (2024).
- ²² S. McArdle, T. Jones, S. Endo, Y. Li, S. C. Benjamin, and X. Yuan, *npj Quantum Inf.* **5**, 75 (2019).
- ²³ T. H. Kyaw, M. B. Soley, B. Allen, P. Bergold, C. Sun, V. S. Batista, and A. Aspuru-Guzik, *Quantum Sci. Technol.* **9**, 01LT01 (2023).
- ²⁴ R. Dutta, D. G. Cabral, N. Lyu, N. P. Vu, Y. Wang, B. Allen, X. Dan, R. G. Cortiñas, P. Khazaei, S. E. Smart, *et al.*, *J. Chem. Theory Comput.* **20**, 6426 (2024).
- ²⁵ R. Dutta, N. P. Vu, C. Xu, D. G. Cabral, N. Lyu, A. V. Soudackov, X. Dan, H. Li, C. Wang, and V. S. Batista, *J. Chem. Theory Comput.* **21**, 2281 (2025).
- ²⁶ C. Weedbrook, S. Pirandola, R. García-Patrón, N. J. Cerf, T. C. Ralph, J. H. Shapiro, and S. Lloyd, *Rev. Mod. Phys.* **84**, 621 (2012).
- ²⁷ G. Verdon, J. M. Arrazola, K. Brádler, and N. Killoran, arXiv preprint arXiv:1902.00409 (2019).
- ²⁸ Y. Enomoto, K. Anai, K. Udagawa, and S. Takeda, *Phys. Rev. Res.* **5**, 043005 (2023).
- ²⁹ F. Khosravi, A. Scherer, and P. Ronagh, in *2023 IEEE International Conference on Quantum Computing and Engineering (QCE)*, Vol. 1 (IEEE, 2023) pp. 184–195.
- ³⁰ P. Chandarana, K. Paul, M. Garcia-de Andoin, Y. Ban, M. Sanz, and X. Chen, *Commun. Phys.* **7**, 315 (2024).
- ³¹ J. L. O’Brien, A. Furusawa, and J. Vučković, *Nat. Photonics* **3**, 687 (2009).
- ³² J. Wang, F. Sciarrino, A. Laing, and M. G. Thompson, *Nat. Photonics* **14**, 273 (2020).
- ³³ J. M. Arrazola, V. Bergqhm, K. Brádler, T. R. Bromley, M. J. Collins, I. Dhand, A. Fumagalli, T. Gerrits, A. Goussev, L. G. Helt, *et al.*, *Nature* **591**, 54 (2021).
- ³⁴ A. Blais, A. L. Grimsmo, S. M. Girvin, and A. Wallraff, *Rev. Mod. Phys.* **93**, 025005 (2021).
- ³⁵ A. Copetudo, C. Y. Fontaine, F. Valadares, and Y. Y. Gao, *Appl. Phys. Lett.* **124**, 080502 (2024).

³⁶ V. Sivak, A. Eickbusch, B. Royer, S. Singh, I. Tsoutsios, S. Ganjam, A. Miano, B. Brock, A. Ding, L. Frunzio, *et al.*, *Nature* **616**, 50 (2023).

³⁷ B. L. Brock, S. Singh, A. Eickbusch, V. V. Sivak, A. Z. Ding, L. Frunzio, S. M. Girvin, and M. H. Devoret, arXiv preprint arXiv:2409.15065 (2024).

³⁸ S. Krastanov, V. V. Albert, C. Shen, C.-L. Zou, R. W. Heeres, B. Vlastakis, R. J. Schoelkopf, and L. Jiang, *Phys. Rev. A* **92**, 040303 (2015).

³⁹ A. Eickbusch, V. Sivak, A. Z. Ding, S. S. Elder, S. R. Jha, J. Venkatraman, B. Royer, S. M. Girvin, R. J. Schoelkopf, and M. H. Devoret, *Nat. Phys.* **18**, 1464 (2022).

⁴⁰ A. A. Diringer, E. Blumenthal, A. Grinberg, L. Jiang, and S. Hacohen-Gourgy, *Phys. Rev. X* **14**, 011055 (2024).

⁴¹ X. You, Y. Lu, T. Kim, D. M. Kurkcuoglu, S. Zhu, D. van Zanten, T. Roy, Y. Lu, S. Chakram, A. Grassellino, A. Romanenko, J. Koch, and S. Zorzetti, arXiv preprint arXiv:2403.00275 (2024).

⁴² B. Zhang and Q. Zhuang, *Quantum Sci. Technol.* **10**, 015009 (2024).

⁴³ Y. Liu, S. Singh, K. C. Smith, E. Crane, J. M. Martyn, A. Eickbusch, A. Schuckert, R. D. Li, J. Sinanan-Singh, M. B. Soley, *et al.*, arXiv preprint arXiv:2407.10381 (2024).

⁴⁴ C. S. Wang, J. C. Curtis, B. J. Lester, Y. Zhang, Y. Y. Gao, J. Freeze, V. S. Batista, P. H. Vaccaro, I. L. Chuang, L. Frunzio, L. Jiang, S. M. Girvin, and R. J. Schoelkopf, *Phys. Rev. X* **10**, 021060 (2020).

⁴⁵ F. Glover, G. Kochenberger, and Y. Du, arXiv preprint arXiv:1811.11538 (2018).

⁴⁶ F. Glover, G. Kochenberger, and Y. Du, in *The Quadratic Unconstrained Binary Optimization Problem: Theory, Algorithms, and Applications* (Springer, 2022) pp. 39–56.

⁴⁷ A. Lucas, *Front. Phys.* **2**, 5 (2014).

⁴⁸ S. Mücke, N. Piatkowski, and K. Morik, in *LWDA* (2019) pp. 144–155.

⁴⁹ R. A. Quintero and L. F. Zuluaga, Techn. Ber. Technical Report. Department of Industrial and Systems Engineering, Lehigh University (2021).

⁵⁰ T. Bontekoe, F. Phillipson, and W. v. d. Schoot, in *International Conference on Computational Science* (Springer, 2023) pp. 90–107.

⁵¹ S. Martello and P. Toth, *Knapsack problems: Algorithms and computer implementations* (John Wiley & Sons, 1990).

⁵² S. Martello and P. Toth, *Oper. Res.* **45**, 768 (1997).

⁵³ S. Martello, D. Pisinger, and P. Toth, *Manag. Sci.* **45**, 414 (1999).

⁵⁴ D. Pisinger, *Comput. Oper. Res.* **32**, 2271 (2005).

⁵⁵ H. M. Salkin and C. A. De Kluyver, *Nav. Res. Logist. Q.* **22**, 127 (1975).

⁵⁶ I. Yevseyeva, E. B. Lenselink, A. de Vries, A. P. IJzerman, A. H. Deutz, and M. T. Emmerich, *Inf. Sci.* **475**, 29 (2019).

⁵⁷ Y. Wang, Z. Hu, B. C. Sanders, and S. Kais, *Front. Phys.* **8**, 589504 (2020).

⁵⁸ N. Metropolis, A. W. Rosenbluth, M. N. Rosenbluth, A. H. Teller, and E. Teller, *J. Chem. Phys.* **21**, 1087 (1953).

⁵⁹ W. K. Hastings, *Biometrika* **57**, 97 (1970).

⁶⁰ N. Mohseni, P. L. McMahon, and T. Byrnes, *Nat. Rev. Phys.* **4**, 363 (2022).

⁶¹ Y. Liu, J. Sinanan-Singh, M. T. Kearney, G. Mintzer, and I. L. Chuang, *Phys. Rev. A* **104**, 032605 (2021).

⁶² J. R. Johansson, P. D. Nation, and F. Nori, *Comput. Phys. Commun.* **183**, 1760 (2012).

⁶³ P. Virtanen, R. Gommers, T. E. Oliphant, M. Haberland, T. Reddy, D. Cournapeau, E. Burovski, P. Peterson, W. Weckesser, J. Bright, *et al.*, *Nat. Methods* **17**, 261 (2020).

⁶⁴ A. Javadi-Abhari, M. Treinish, K. Krsulich, C. J. Wood, J. Lishman, J. Gacon, S. Martiel, P. D. Nation, L. S. Bishop, A. W. Cross, B. R. Johnson, and J. M. Gambetta, “Quantum computing with Qiskit,” (2024), arXiv:2405.08810 [quant-ph].

⁶⁵ J. Weidenfeller, L. C. Valor, J. Gacon, C. Tornow, L. Bello, S. Woerner, and D. J. Egger, *Quantum* **6**, 870 (2022).

⁶⁶ M. A. Nielsen and I. L. Chuang, *Quantum computation and quantum information* (Cambridge university press, 2010).

⁶⁷ M. H. Michael, M. Silveri, R. T. Brierley, V. V. Albert, J. Salmilehto, L. Jiang, and S. M. Girvin, *Phys. Rev. X* **6**, 031006 (2016).

⁶⁸ S. Lee, J. Lee, H. Zhai, Y. Tong, A. M. Dalzell, A. Kumar, P. Helms, J. Gray, Z.-H. Cui, W. Liu, *et al.*, *Nat. Commun.* **14**, 1952 (2023).

⁶⁹ Z. Li, E. Gupta, F. Zhao, R. Banerjee, Y. Lu, T. Roy, A. Oriani, A. Vrajitoarea, S. Chakram, and D. I. Schuster, arXiv preprint arXiv:2503.13953 (2025).

⁷⁰ J. Huang, T. J. DiNapoli, G. Rockwood, M. Yuan, P. Narasimhan, E. Gupta, M. Bal, F. Crisa, S. Garattoni, Y. Lu, *et al.*, arXiv preprint arXiv:2503.10623 (2025).

⁷¹ K. Noh, S. Girvin, and L. Jiang, *Physical Review Letters* **125**, 080503 (2020).

⁷² J. Wu, A. J. Brady, and Q. Zhuang, *Quantum* **7**, 1082 (2023).

⁷³ S. Dutta, D. Biswas, and P. Mandayam, arXiv preprint arXiv:2406.02444 (2024).

⁷⁴ D. Su, R. Israel, K. Sharma, H. Qi, I. Dhand, and K. Brádler, *Quantum* **5**, 452 (2021).

⁷⁵ A. Taylor, G. Bressanini, H. Kwon, and M. Kim, *Phys. Rev. A* **110**, 022622 (2024).

⁷⁶ J. Mills and R. Mezher, arXiv preprint arXiv:2405.02278 (2024).

⁷⁷ Y. Teo, S. Shringarpure, S. Cho, and H. Jeong, arXiv preprint arXiv:2411.11313 (2024).